Case Studies in Thermal Engineering 61 (2024) 105062

Contents lists available at ScienceDirect

Case Studies in Thermal Engineering

journal homepage: www.elsevier.com/locate/csite

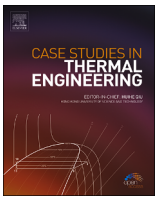

Influence of heating elements layout on temperature uniformity in a large size heat treatment furnace

Sajad Mirzaei [a, *], Nima Bohlooli Arkhazloo [a], Jean-Benoit Morin [b], Mohammad Jahazi [a, **]

[a] Département de Génie Mécanique, École de Technologie Supérieure, Montréal, QC H3C 1K3, Canada
[b] Finkl Steel Inc., 100 McCarthy, Saint-Joseph-de-Sorel, Sorel-Tracy, QC J3R 3M8, Canada

ARTICLE INFO

Handling Editor: Huihe Qiu

Keywords:
Industrial electric furnace
Heat treatment
Temperature uniformity
Optimization
Heating elements layout
CFD simulation

ABSTRACT

Computational Fluid Dynamics simulations were used to optimize heating elements placement on the walls of a large size electrical heat treatment furnace in order to reduce temperature gradients within the furnace and uneven temperatures on different faces of the blocks which could result in variabilities in final mechanical properties. Initial evaluations of different layouts highlighted the effectiveness of equipping two side walls. Subsequently, an optimal percentage of side wall coverage was identified through simulations and multi-objective evolutionary optimization. Genetic and pareto search algorithms yielded 10 % and 14.2 % as optimum values, respectively. Implementing an optimal coverage demonstrated significant reductions in surface temperature non-uniformity, surface-to-center temperature differential, and temperature differences between loaded blocks. These improvements suggest a potential for enhanced uniformity in mechanical properties across a batch of products. This approach presents a promising strategy for obtaining consistent and efficient heat treatment cycles in industrial heat treatment furnaces resulting in energy saving and improved product quality.

1. Introduction

Large size furnaces are widely used in industry for the heat treatment of all kind of alloys (superalloys, aluminum alloys, steels, etc.). The largest number of such furnaces are found in steel industry because of the extensive use of steels when compared to other alloys. Most, if not all, the steels products go through one or several heat treatment cycles and as a result, heat treatment processes are among the main sources of energy consumption and environmental footprints. However, they are mandatory steps of the manufacturing process of high strength steels used in many industries. Therefore, the efficiency of a heat treatment furnace in terms of its energy consumption as well as its capability in producing uniform temperature distribution that affect steel's metallurgical transformations are of critical importance [1]. In their majority, heat treating industrial furnaces use natural gas as the main source of heating; however, in recent years, due to new environmental requirements, the interest towards the use of electric furnaces has significantly increased [2]. Despite their promising future, significant challenges still remain to be addressed from a design perspective, e.g., layout, size, and type of electric heating elements, as well as the impact of electricity-based heating, on the final mechanical properties of the product versus a gas-fired based heating approach. This study has been defined in this context and investigates resistance electric fur-

* Corresponding author.
** Corresponding author.
E-mail address: sajad.mirzaei.1@ens.etsmtl.ca (S. Mirzaei).

https://doi.org/10.1016/j.csite.2024.105062
Received 11 June 2024; Received in revised form 12 August 2024; Accepted 31 August 2024
Available online 2 September 2024
2214-157X/© 2024 The Authors. Published by Elsevier Ltd. This is an open access article under the CC BY-NC license (http://creativecommons.org/licenses/by-nc/4.0/).

naces' design parameters, focusing on the balance between energy efficiency and product quality, and emphasizes the application of computational fluid dynamics (CFD) for furnace thermal analysis.

Extensive work has been conducted in recent years on the application of CFD to optimize different aspects of resistance electric furnaces. For instance, Palacio-Caro et al. examined a pit-type electric steel tempering furnace by CFD, testing fan speeds to improve thermal efficiency. Their study, using a moving-reference frame (MRF) method, revealed the critical role of fan speed in optimizing temperature homogeneity and heat transfer in high-temperature furnaces; however, in their study the impact of heating elements on temperature uniformity in the parts were not considered [3]. Similarly, Smolka et al. conducted transient simulations across 30 different cases using Ansys Fluent to enhance airflow and thermal dynamics in a laboratory-scale drying oven. Adjusting fan speeds and heater placements, they improved temperature uniformity, achieving a reduction in non-uniformity from 4.2 °C to 2.3 °C in the modified prototype under specific conditions. Despite these advancements, the study did not establish a quantitative correlation between the simulation parameters and the resulting temperature uniformity, offering potential directions for future research to optimize device design further [4].

From another aspect, Filipponi et al. highlighted the substantial energy losses in steel industry furnaces during door-opening events using CFD simulations. Their study showed a significant energy loss of 5606 MJ, during a 10-min door opening and related it to convective heat flux [5]. Also, Fu et al. investigated temperature distributions in a laboratory-scale resistance furnace for superalloy heat treatment, using Fluent. They incorporated a dynamic PID control strategy to regulate the furnace temperature. This approach enhanced the model's ability to predict the equilibrium time required for heating superalloys. Although they developed a robust predictive model, Fu et al. did not analyze temperature discrepancies observed between the center and the surface of the bar [6].

Analogously, Angelopoulos et al. developed a CFD model for mineral microsphere expansion in a vertical electric furnace (VEF), examining how furnace wall temperature and air feed rate affected particle states and the final product quality. They reported that increasing the furnace wall temperature under isothermal mode from 900 to 1200 °C reduced microsphere density by 28.7%–43.2 % across different feed rates, emphasizing the critical impact of precise temperature control on the quality of the product. However, their study stops short of addressing the scalability of these findings to industrial operations [7]. In a recent publication, the present authors used CFD, to examine the impact of stacking patterns on temperature uniformity of large size steel blocks and reported that optimal spacer and skid sizes could reduce temperature non-uniformities by at least 24 %. The CFD predictions were validated experimentally; thereby, demonstrating, CFD's efficacy in predicting transient temperatures and optimizing industrial settings [8].

Furnace design optimization studies using 3D CFD by Tan et al. resulted in reducing heat losses by at least 22 % in a vertical wafer annealing furnace [9]. In another study, Díaz-Ovalle et al. employed CFD by Ansys CFX to assess the influence of baffle plate geometries on heating efficiency in a convective electric oven, connecting baffle design with enhanced energy utilization and uniform baking conditions. However, their analysis did not quantify the temperature uniformity and preheating time improvements, and simulations were conducted without considering the effects of load, which could alter oven performance in real-world conditions [10].

The present work focuses on the optimization of heating elements layout and the use of evolutionary algorithms to improve resistance electric furnace efficiency. To this end, a 3D computational fluid dynamics model featuring complex features such as axial fans and the heating elements was utilized to simulate the tempering process of high strength steel blocks. The simulation results were then validated experimentally at the industrial scale to test the reliability of the predictions. In a third step, genetic and pareto search algorithms were utilized to refine the layout, securing enhanced temperature uniformity within the furnace and through the thickness of the heat-treated steel blocks.

Nomenclature			
CFD	Computational fluid dynamics	C_p	Specific heat (J kg^{-1} K^{-1})
VEF	Vertical Electric Furnace	S	Heat sources (J m^{-3} s^{-1})
PID	Proportional–integral–derivative	k	Thermal conductivity (W m^{-1} K^{-1})
TSWE	Two Side Walls Equipped	x	Independent variable
AFWE	All Four Walls Equipped	y	Dependent variable
AWICE	All Walls Including Ceiling Equipped	n	Degree of polynomial
OCE	Only Ceiling Equipped	$F_i(x)$	Objective function
UB	Upper block	i	Function index
LB	Lower block	x^*	Reference point
P	Power (kW)	*R-sq*	Root square (%)
V	Voltage (v)	*MSE*	Mean square error
Hz	Frequency (Hz)	*GA*	Genetic Algorithm
t	Time (s)	*e*	Error term
DO	Discrete ordinates	*PS*	Pareto Search
RTE	Radiative transfer equation	**Greek Letter**	
TC	Thermocouple	v	Velocity vector (m s^{-1})
norm	Normalized value	ρ	Density (kg m^{-3})
I	Radiative intensity	β	Constant coefficients
T	Temperature (°C)	ε	Dissipation rate
p	Pressure	a	Absorption coefficient
N	Number of decision variables	σ	Stefan-Boltzmann constant

2. Furnace and experimental measurements description

The current study was conducted on an industrial electrical heat treatment furnace situated at Finkl Steel in Sorel, Quebec, Canada [11]. This batch-type car bottom furnace boasts a total power capacity of 1710 kW and features two sets of heating elements placed on the opposing side walls of the heating chamber, which collectively encompass 70 % of each side wall's surface area. The furnace design incorporates three axial fans positioned atop the chamber, facilitating the circulation of heated air within and around the treated blocks. These fans maintain a consistent rotational speed of 1750 rpm. Notably, the airflow in these high-temperature fans follows a path through the blades, running parallel to the mounting shaft.

Fig. 1 provides a visual representation of the electric furnace, accompanied by detailed diagrams illustrating the heating chamber's dimensions and key features. The internal dimensions of the furnace's heating chamber span 3.43 m, 4.11 m, and 8.02 m. The loading pattern consists of two large rectangular parallelepiped-shaped forging blocks stacked on top of each other. The upper block (UB) has dimensions of 4.25 × 1.34 × 0.66 m^3, while the lower block (LB) measures 4.6 × 1.27 × 0.63 m^3, each weighing about 29 metric tons. Five steel skids are used to support the placement of these forged blocks on the car bottom of the furnace. This configuration provides insight into the heat treatment of high thickness forging blocks, which is particularly challenging [12].

Circulation of the fluid flow by the fans facilitates product heating, and the furnace is designed without an exhaust system. To maintain insulation, the furnace walls are enveloped by insulating blankets made from spun Fiberfrax ceramic fibers [13], featuring a thickness of 0.254 m and a thermal conductivity of 0.16 W/mK at the tempering temperature of 537 °C.

In conjunction with the 6 thermocouples integrated into the furnace controller system, 5 pre-calibrated K-type thermocouples with stainless steel sheathing were positioned on various points of the steel blocks' surfaces, as illustrated in Fig. 2. Thus, 'L' and 'l' denote the lengths of the lower and upper blocks, respectively; 'H' and 'h' represent their heights; and 'W' and 'w' indicate the widths of the blocks. According to the ISA Standard [14], the K-type thermocouples enveloped in a stainless steel sheath have an accuracy level of ±2.2 °C or ±0.75 % within furnace operating temperatures. Comprehensive insights into the frameworks designed to achieve robust data collection are presented in recent publications by Arkhazloo et al. [12,15,16].

Furthermore, Fig. 3 visually depicts the dynamic evolution of the electrical energy consumption profile of the loaded furnace throughout the heat treatment procedure at a power of 600 V and 60 Hz frequency. It is essential to note that the accuracy of the curve in Fig. 3 is closely tied to the furnace control systems capability to collect data every 10 s, highlighting the systems impact on monitoring and adjusting energy consumption. The changing slope of the curve over time indicates variations in power consumption rate, with the initial steep slope suggesting high power usage, while the gradually leveling slope towards the end signifies a transition to a more constant and stable power consumption rate. This transition reflects the furnace's operational adjustments as it reaches an isothermal state in the heat treatment process.

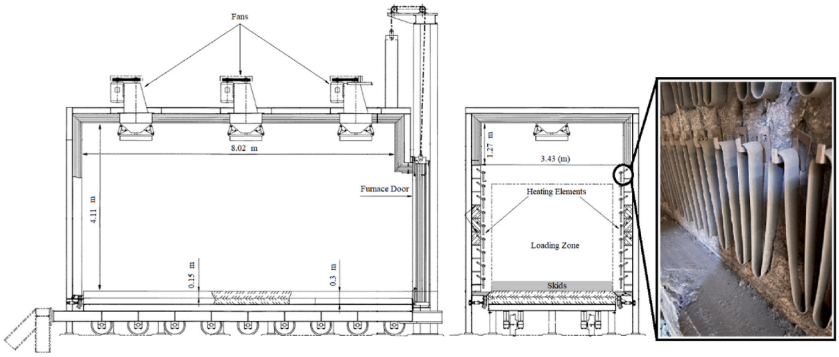

Fig. 1. Industrial electrical heat treatment furnace structure [11].

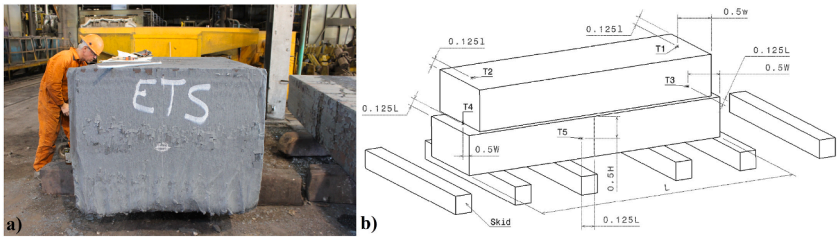

Fig. 2. a) Instrumented high strength steel block b) a schematic view of the five thermocouples' locations.

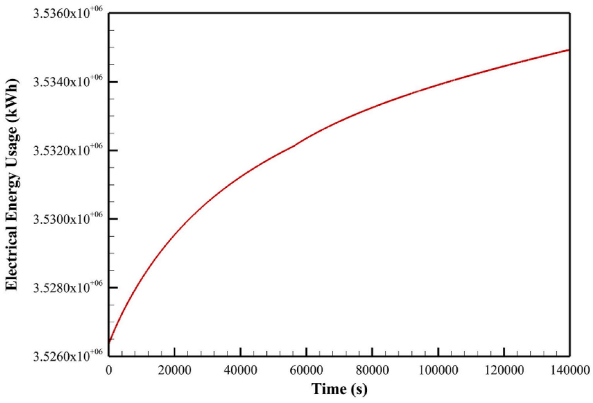

Fig. 3. Dynamic evolution of the electrical energy consumption profile.

3. Heating elements layouts

The analysis of the heating elements layout was conducted in two distinct phases. In Phase 1, a methodical exploration of various scenarios was conducted, involving the strategic arrangement of heating elements across different configurations of furnace walls available in the literature [17]. This phase aimed to identify the impact of heating the stacked high thickness blocks from different directions on thermal uniformity compared to the original condition. The four applicable heating elements layouts subjected to testing were.

1. Two Side Walls Equipped (TSWE), representing the current furnace setup with 70 % of the surface area of each side wall covered by heating elements (original condition used for experimental validation, referred to as TSWE-70);
2. All Four Walls Equipped (AFWE), encompassing both sides, the back wall, and the door, with 70 % of the surface area of each wall covered by heating elements;
3. All Walls Including Ceiling Equipped (AWICE), with 70 % of each of the four walls plus the whole ceiling covered by heating elements;
4. Only Ceiling Equipped (OCE), with the whole ceiling covered by heating elements and none of the side walls equipped.

Phase 2 was focused on determining the optimum percentage of side wall coverage by the heating elements. This phase aimed to fine-tune the area of the side walls being covered by heating elements to optimize thermal uniformity while maintaining the current setup, which is more favorable for industrial partners due to its practicality and cost-effectiveness. Within this phase, seven distinct cases were simulated, each embodying varying coverage percentages identified as TSWE-10, -20, −30, −50, −70, −90, and −100. In each simulation case, the TSWE values represent the percentage of the furnace side walls covered by heating elements. As the TSWE value increases, it signifies a greater area of the side walls being covered, resulting in more extensive exposure of the furnace's interior to the heating elements. The only independent variable in Phase 2 was the surface area of wall coverage. In Fig. 4, a schematic representation of the simulated geometries is presented.

4. Computational details

The methodology integrates computational fluid dynamics modeling, polynomial regression, and advanced optimization algorithms. It must be mentioned that an almost similar approach has been previously applied by other researchers to analyze electrical arc furnaces [18], yet its application to heat treatment furnaces has not been previously reported. The details related to each method are presented in the following.

4.1. CFD model development

Based on the developed CAD model including described details in section 2, three sets of poly-hex core computational grids, namely coarse, medium, and fine, were tested to ensure grid independence of the obtained results. The medium computational grid, comprising about 1.47 million cells as shown in Fig. 5, was found to offer predictions that were closely aligned with the fine computational grids and thus was chosen for subsequent simulations. The developed poly-hex core computational grids using ANSYS Fluent Mosaic Technology [19], incorporating three boundary layers, balanced computational cost and simulation accuracy. The poly-hex core mesh technology provides the advantage of higher computational efficiency due to its reduced cell count and improved orthogonality [20]. The minimum orthogonal quality of the computational grids was 0.1, ensuring adequate accuracy for the simulations.

The furnace power consumption profile shown in Fig. 3, divided by the total surface area of the considered heating elements in each case, was applied as the input energy profile boundary condition. Additionally, an average heat loss value of 594 W/m^2, calculated based on the approach proposed by Hadala et al. [21] and the furnace specifications detailed in section 2, was used as the boundary condition for the furnace walls.

Simulations were conducted using Ansys Fluent 2022, which utilizes the finite volume method for computational analysis [22]. This study specifically focused on heat transfer under turbulent flow conditions induced by fan rotation. The fundamental governing

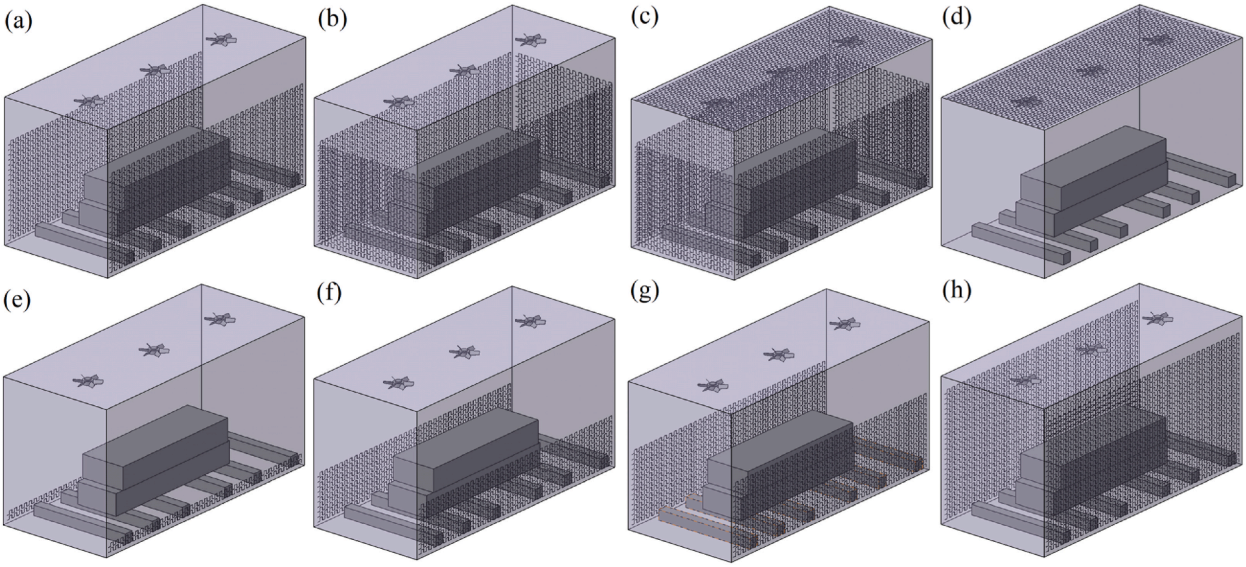

Fig. 4. Comparative geometries under investigation: a) TSWE-70 (original condition), b) AFWE, c) AWICE, d) OCE, e) TSWE-10, f) TSWE-30, g) TSWE-50, and h) TSWE-90.

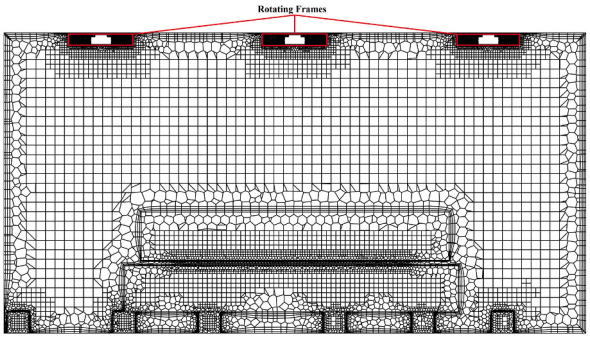

Fig. 5. Computational grid at the central cross-section (furnace side view) of the study domain.

equations employed in the simulation were the continuity equation, the Navier-Stokes equation for momentum, and the energy equation, as detailed in equations (1)–(3) [22]. Consequently, to handle the pressure-velocity coupling in this complex flow scenario, the SIMPLEC algorithm was adopted which offers a more consistent and rapid convergence [23].

Continuity Equation:

$$\frac{\partial \rho}{\partial t} + \nabla.(\rho v) = 0 \tag{1}$$

Momentum Equation:

$$\frac{\partial (\rho v)}{\partial t} + \nabla.\rho vv = -\nabla p + \rho g + \nabla.\tau \tag{2}$$

Energy Equation:

$$\frac{\partial}{\partial t}(\rho e) + \nabla.(v(\rho e + p)) = \nabla.(k\nabla T) + S \tag{3}$$

Here, ρ is the fluid density, p is the pressure, v is the velocity field, g represents the gravitational acceleration, τ is the stress tensor, e is the total energy per unit mass, which includes both kinetic and internal energy, T is the temperature, k is the thermal conductivity and S encompasses radiation and other heat sources.

In the present work, the turbulence associated with the induced flow circulation caused by fans rotation was modeled using the two-equation realizable k-ε turbulence model [24] in conjunction with the multiple reference frame (MRF) model [22]. This was achieved by considering cylindrical-shaped zones around each of the fans inside the furnace where the MRF model was applied. The computational domain was divided into three rotating reference frames corresponding to the three fans and one stationary frame for

the rest of the furnace, including the blocks. The MRF approach transforms the fluid equation of motion to a rotating frame, enabling steady-state solutions for rotating parts of the domain [8]. The governing equations for the MRF zones include modifications to the Navier-Stokes equations to account for rotational effects [22].

To accurately capture the near-wall effects, scalable wall functions were employed in conjunction with the realizable k-ε model. This approach improves the accuracy of turbulence modeling close to the walls, where flow characteristics are significantly different from the bulk flow. The scalable wall functions ensure that the near-wall treatment is appropriate across a wide range of Y^+ numbers and flow conditions [20].

This combination of the realizable k-ε model and the MRF model allows for capturing both the large-scale rotational flows induced by the fans and the finer turbulence structures within the furnace. For the turbulence model, this is achieved by solving the equations for turbulence kinetic energy (k) and dissipation rate (ε), as outlined in Eqs. (4) and (5). It uses a different formulation for the turbulent viscosity and the constants $C_{1\varepsilon}$ and $C_{2\varepsilon}$ compared to the standard k-ε model. These modifications make the Realizable model more accurate for a wider range of turbulent flows [24]. It must be noted that the above approach is in agreement with studies by other researchers [3,4,10,25] who reported that k-ε and MRF could be reliably used to study turbulent flow under conditions closely resembling present work.

$$\frac{\partial(\rho k)}{\partial t} + \nabla.(\rho k v) = \nabla.\left[\left(\mu + \sigma_k \mu_t\right)\nabla \mathrm{k}\right] + P_k - \rho\varepsilon \tag{4}$$

$$\frac{\partial(\rho \varepsilon)}{\partial t} + \nabla.(\rho \varepsilon v) = \nabla.\left[\left(\mu + \sigma_\varepsilon \mu_t\right)\nabla \varepsilon\right] + C_{1\varepsilon}\frac{\varepsilon}{k}P_k - C_{2\varepsilon}\rho\frac{\varepsilon^2}{k} \tag{5}$$

Here, k is the turbulent kinetic energy per unit mass, μ is the molecular viscosity, μ_t is the turbulent viscosity. σ_k is the turbulent Prandtl number, P_k is the production of turbulent kinetic energy, ε is the turbulent dissipation rate, σ_ε is the turbulent Prandtl number for ε, $C_{1\varepsilon}$ and $C_{2\varepsilon}$ are model constants.

Among the radiation models reported [26] by Versteeg for calculating radiative heat transfer in a 3-dimensional furnace geometry, the S_{16} discrete ordinates (DO) method has an acceptable accuracy level, comparable to the Monte Carlo (MC) method. However, the MC method demands substantially more computational resources, over 20 times greater than the DO method. In the S_n DO model, the 'n' denotes the number of discrete angular directions used in the numerical approximation of the radiative transfer equation. Jamaluddin and Smith [27] tested different approximation orders (S_2, S_4, S_6, and S_8) for the DO model in a 3D rectangular enclosure, aiming to evaluate their effectiveness against exact analytical and numerical solutions. The S_4 approximation was deemed adequate, considering its balance between accuracy and computational time. Although the surface to surface (S2S) model was previously used for the same geometry by Mirzaei et al. and they reached an acceptable average error of 6.6 % [8]. However, for considering the radiation effects in the present work, the S4 DO model following Jamaluddin and Smith tests [27] was adopted in this study. This model provides a numerical solution to the radiative transfer equation (RTE) over a limited set of discrete solid angles, which can be mathematically expressed as [22]:

$$\nabla.\left(I\left(\vec{r},\vec{s}\right)\vec{s}\right) + a\mathrm{I}\left(\vec{r},\vec{s}\right) = a\frac{\sigma T^4}{\pi} \tag{6}$$

Where I denotes the radiative intensity at position $\vec{r}$ in direction $\vec{s}$, a is the absorption coefficient, and σ stands for the Stefan-Boltzmann constant.

The ideal gas model was employed to account for variations in air density due to temperature changes, while keeping pressure constant. This model is appropriate for the current study as it simplifies the calculations and is sufficiently accurate for the temperature range considered in the simulations [28]. The ideal gas assumption facilitates efficient computation without significant loss of accuracy, given the relatively constant pressure conditions within the furnace.

Notably, in addressing the challenges of heat treatment processes, this study specifically considered the impact of temperature variations on the thermo-physical properties of large blocks made of high-strength medium carbon steel. Utilizing JMatPro software [29], an application proficient in calculating properties for complex alloys, these varying properties were estimated and subsequently incorporated into the CFD model, as illustrated in Fig. 6. The accurate chemical composition of the material, measured by the authors' team and presented in Table 1, served as the input for the JMatPro software. The robustness of JMatPro in accurately determining the properties for such specific alloy compositions has been corroborated in the existing literature [15,30,31] and aligns with the findings from previous investigations by the authors [8].

In this simulation, particular attention was given to the temperature-dependent thermal conductivity and specific heat, critical parameters for precisely modeling the heat conduction within the steel blocks and ensuring the system's energy equilibrium. In Fig. 6, the green curve represents thermal conductivity, which shows a slight initial increase, peaks at approximately 140 °C with a value of 41.5 W/m.K, and then progressively decreases as the temperature rises, stabilizing at about 35.2 W/m.K during the isothermal phase of the tempering process. Conversely, the specific heat exhibits a consistent upward trend from ambient temperature to the final target tempering temperature of 537 °C, increasing from 450 J/kg.K to approximately 752 J/kg.K. It is important to highlight that in simulations involving fluid-solid interactions, as well as metallurgical and thermal domains that necessitate physically coupled models, the precision of the numerical simulation is critically dependent on pre-calculated, temperature-dependent variables [32,33]. These are closely associated with the phases present in the steel and their transformation throughout the process [34].

For the convergence criteria, values of 10^{-5} were set for the continuity, momentum, and turbulence equations, while a finer 10^{-6} threshold was applied to the energy and radiation equations, ensuring accurate and stable simulation outcomes.

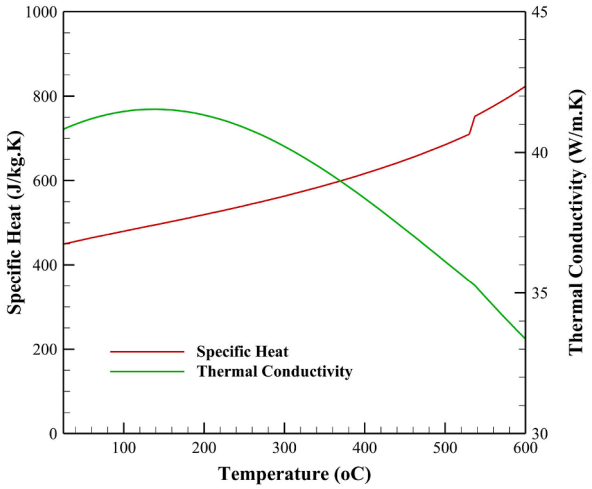

Fig. 6. Temperature dependent thermo-physical properties of large blocks.

Table 1
Chemical composition of the investigated steel (wt%).

C	Mn	Si	Ni	Cr	Mo	Cu	Other
0.35	0.99	0.41	0.5	1.86	0.53	0.16	Micro Alloying

4.2. Polynomial regression fitting

Once the CFD simulations provided results for different scenarios, the relationship between the TSWE values and the furnace performance parameters (surface temperature non-uniformity, surface-to-center temperature differential, centers temperature differential) was quantified using polynomial regression of degree 3. The general form of a polynomial regression is [35]:

$$y_x = \beta_0 + \beta_1 x + \beta_2 x^2 + \ldots + \beta_n x^n + e \tag{7}$$

Where y_x is the dependent variable (e.g., surface temperature non-uniformity), x is the independent variable (e.g., wall coverage percentage), n is the polynomial degree, β′s are the coefficients that characterize the magnitude and direction of the influence of each term, and e is the error term.

To ensure the regression models are comparable despite differing scales of the parameters, the extracted values from the CFD simulations were normalized. The normalization process adjusts the scale of each parameter, facilitating direct comparison for optimization purposes. The normalized values were calculated using the equation:

$$\text{Normalized Value} = y_x - y_{min} / y_{max} - y_{min} \tag{8}$$

MATLAB 2021 tools were employed to fit these polynomial functions to the normalized data points obtained from CFD simulations, enabling predictive insights into furnace behavior under different conditions.

4.3. Multi-objective optimization

To determine the optimal layout based on the derived polynomial relationships, two evolutionary optimization algorithms were employed:

Genetic Algorithm (GA) is well known for obtaining optimal solutions by emulating the process of natural evolution [36]. The algorithm starts with an initial population of potential solutions, evaluates their fitness, and iteratively refines the population through processes analogous to selection, crossover (recombination), and mutation. The ‘crossover heuristic’ function was employed as the crossover function. This particular method was chosen because it is specifically tailored for multi-objective optimization [37]. This method enhances variation among the solutions, broadening the search across the solution space and increasing the likelihood of identifying optimal solutions for each objective in multi-objective optimization scenarios [37]. The approach to minimizing the objective functions is inspired by methodologies outlined in ‘Multi-objective Evolutionary Optimization for Product Design and Manufacturing’ [38]. Table 2 provides an overview of the hyperparameters used in the implemented genetic algorithm.

Pareto search (PS) algorithm was also used; it is characterized by its unique ability to effectively identify and differentiate Pareto optimal solutions in multi-objective optimization contexts [35], which is complementary to the GA method and therefore will allow a more accurate analysis of the results. In this methodology, the ‘GPSPositiveBasis2N′ polling strategy for the PS algorithm was selected specifically. This choice was made due to its systematic utilization of 2N positive basis vectors in each iteration of the PS algorithm. The ‘GPSPositiveBasis2N′ method is adept at navigating one-dimensional search spaces [35], which aligns well with the requirements of the current problem. By employing this strategy, it was aimed to enhance the capability of the PS algorithm in identifying poten-

Table 2
GA hyperparameters.

Max Generations	1000
Population Size	500
Crossover Fraction	0.6
Crossover function	Crossover heuristic
Pareto Fraction	0.4
Function Tolerance	1e-6

tially superior solutions, thereby optimizing the effectiveness of the algorithm in this specific context. Given a set of objective functions F = {$f_1(x)$, $f_2(x)$, …, $f_i(x)$}, a solution x^* is Pareto optimal if there is no x such that [39]:

$$f_i(x) \leq f_i(x^*) \quad \forall i \tag{9}$$

and

$$f_i(x) \leq f_i(x^*) \tag{10}$$

for at least one j. Table 3 outlines the hyperparameters for the applied Pareto search algorithm.

By cohesive blending these tools and techniques, the study pinpointed the layouts that significantly elevated the furnace's performance, achieving enhanced uniformity in temperature distribution and other desired quality parameters.

5. Results and discussion

5.1. Validation

Fig. 7 provides a comparative representation, expressed in percentage, of the transient temperatures observed on the surfaces of the forging blocks for different thermocouple (TC) locations and the corresponding predictions obtained from the CFD model. The error percentage shown in this figure reflects the accuracy of the TSWE-70 model, which represents the original condition of the furnace where the experimental test was conducted. In this original condition, 70 % of the furnace side walls were covered by heating elements, hence the designation TSWE-70.

Over the entire 41.6-h duration of the heat treatment process, the CFD predictions present consistency when compared with the actual measurements showcasing a maximum average deviation of approximately 2 % (attributed to TC5) further confirming the ro-

Table 3
PS algorithm hyperparameters.

Max Function Evaluations	24000
Pareto Set Size	200
Min Poll Fraction	0.5
Poll Method	GPSPositiveBasis2N
Pareto Set Change Tolerance	1e-6
Max Iterations	1000

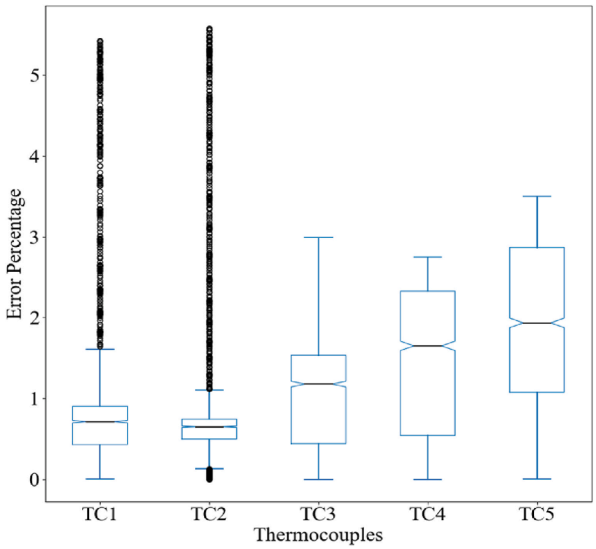

Fig. 7. Validation of the CFD model.

bustness of the developed CFD model within the scope of this investigation. The outlier circles for TC1 and TC2 indicate instances where the model's predictions varied from the empirical data by a margin that is larger (and notably smaller for TC2) than the typical variation observed. These outliers, while exceeding the main error range, maintain an error below 6 percent, thereby supporting the overall accuracy of the simulation.

This validation paved the way for the model's utilization in assessing the influence of heating elements layout on the thermal history of the large-size blocks under scrutiny. Subsequently, nine other models were developed and assessed to evaluate different heating element configurations: AFWE, AWICE, OCE, TSWE-10, TSWE-20, TSWE-30, TSWE-50, TSWE-90, and TSWE-100.

5.2. Phase-1 analysis

Fig. 8 illustrates the volume average temperature profiles, or in other words, the heating curves experienced by both large blocks over the tempering process in layout TSWE-70 (original condition). The blue dashed line represents the temperature of the upper block (UB), while the black dashed line denotes the lower block (LB). Initially, the blocks exhibit different volume average temperatures due to their distinct initial conditions, with the lower block starting at a slightly higher temperature than the upper block.

Throughout the non-isothermal cycle, both blocks progressively absorb heat. The upper block (UB) shows a steeper initial rise in temperature, indicating a more rapid heat absorption compared to the lower block (LB). However, as time progresses, the rate of temperature increases for both blocks start to converge. Around the 100,000-s mark, both blocks reach approximately 530 °C, and their temperature profiles begin to level off as they approach the target temperature for the isothermal cycle. During the subsequent isothermal cycle, both blocks maintain the target temperature, demonstrating more uniform thermal conditions for the remainder of the process. This phase is crucial for achieving the desired mechanical properties in the tempered steel, as it ensures that the blocks are held at a consistent temperature.

This analysis underscores the intense thermal behaviors in the initial phase (non-isothermal cycle), which lead to some temperature non-uniformities. The distinct heating rates in the early stages can be attributed to the varying direct exposure each block receives from the respective heating elements. These dynamics are further discussed in Fig. 9, which delve into the temperature distributions and uniformity across different heating element configurations.

Notably, the volume average temperature profiles indicate that the current TSWE-70 setup effectively brings both blocks to the desired temperature, but the differences highlight potential areas for optimization in the heating process to minimize temperature gradients and improve overall uniformity.

In Fig. 9(a), the transient changes in maximum surface temperature non-uniformities of large blocks during heat treatment across four layouts from phase 1 are depicted. The surface temperature non-uniformity is defined as the instantaneous temperature difference between two points on a block's surface, with one having the highest and the other the lowest temperature. Notably, significant non-uniformities were observed during heat treatment, aligning with findings for gas-fired furnaces [40–42]. Metallurgical heat treatment studies usually overlook this non-uniformity, focusing more on the temperature gradient from the block's surface to its center.

In layout AWICE, where all four walls and the ceiling were equipped with heating elements, the non-uniformities surged to a notable 212 °C around the upper block, increasing at rates up to 76.5 °C/h. Other layouts, particularly TSWE-70, recorded lower non-uniformities at 200 °C. By the end of the process, non-uniformities decreased, aligning with the isothermal tempering temperature of 537 °C. However, prolonged exposure to these non-uniformities could impact the mechanical properties across the product, as a large value for surface non-uniformities indicates different thermal histories experienced by one end of the block compared to the other. This variation is directly correlated with the final mechanical properties of the product, as discussed in the literature [43,44].

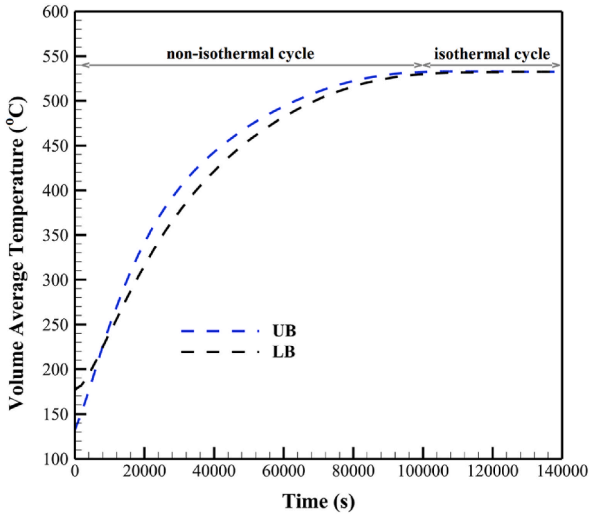

Fig. 8. Volume average temperature profiles of upper (UB) and lower (LB) blocks in layout TSWE-70.

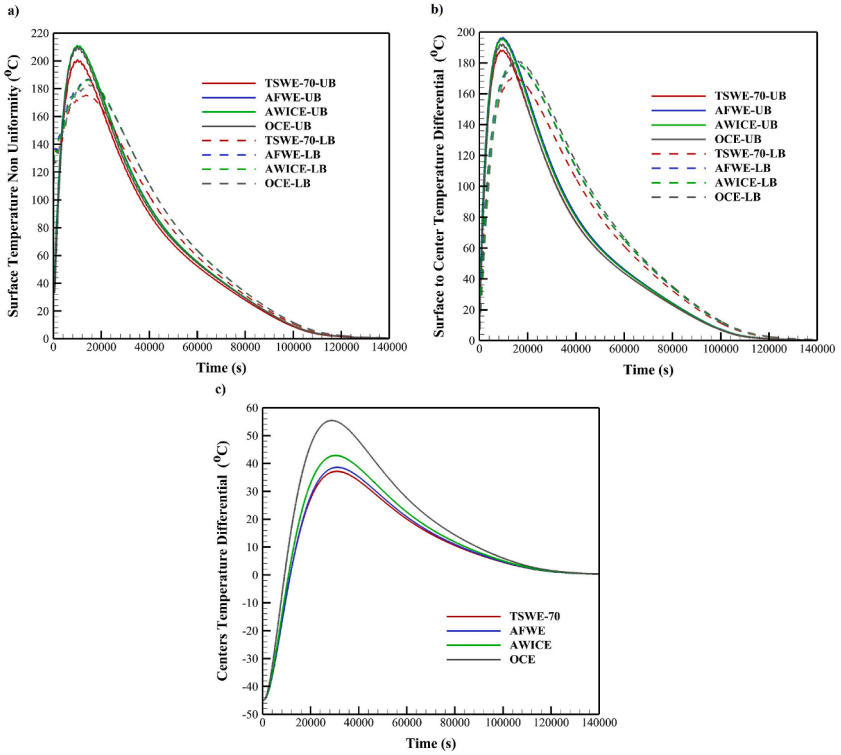

Fig. 9. Comparative thermal dynamics of upper (UB) and lower blocks (LB) during heat treatment: analysis of a) surface temperature non-uniformity, b) surface-to-center temperature differentials, and c) centers temperature differential under four heating elements layouts.

The initial peak in surface temperature non-uniformity is most pronounced in the AWICE and AFWE configuration, reaching the maximum early in the process. This indicates that equipping all walls and the ceiling with heating elements leads to more rapid but uneven heating. The curves for OCE and TWSE-70 configurations also show significant initial non-uniformities, but these reduce more quickly compared to AWICE and AFWE. The TSWE-70 configuration, on the other hand, shows a relatively lower initial non-uniformity, suggesting a more controlled and uniform heating process.

The total surface temperature non-uniformity (surface area under each curve) for both blocks is notably less in TSWE-70. This indicates the advantage of the TSWE-70 configuration in maintaining more consistent surface temperatures throughout the heat treatment process. Additionally, the rate at which the non-uniformity decreases provides insights into the thermal stability of each configuration. For instance, the faster reduction of non-uniformities in the TSWE-70 layout implies a quicker stabilization of temperature differences, which is beneficial for achieving uniform thermal conditions.

Fig. 9(b) illustrates the transient changes in the surface-to-center temperature differential of each block during phase 1. The surface-to-center temperature differential of each block is calculated as the immediate temperature difference between the block's hottest surface point and its center point.

TSWE-70 outperforms, with the smallest differential at 188 ˚C and 170 ˚C for both upper and lower blocks, respectively. In contrast, the highest differentials for the lower and upper blocks are observed in layouts OCE and AFWE, respectively. This indicates that these layouts lead to rapid but uneven internal heating, causing significant temperature gradients within the blocks. The curves for TSWE-70 show a more controlled rise, having a notably smoother and lower peak, suggesting better internal thermal uniformity. The difference can be attributed to the direct exposure each block receives from the respective heating elements.

Comparing this with Fig. 9(a), it is evident that the TSWE-70 configuration not only minimizes surface temperature non-uniformity but also reduces internal temperature gradients, which is crucial for achieving uniform mechanical properties. The AFWE and AWICE layouts, while showing high surface temperature non-uniformity in Fig. 9(a) for the upper block, also exhibit significant surface-to-center temperature differentials in Fig. 9(b), indicating their inefficiency in achieving uniform heating.

The rate at which the surface-to-center temperature differential decreases provides insights into the thermal stability of each configuration. The fast reduction of temperature differentials in the TSWE-70 layout implies a quicker stabilization of internal temperature differences, beneficial for achieving uniform thermal conditions throughout the block. This aligns with observations from Fig. 9 (a), where TSWE-70 also showed a faster reduction in surface temperature non-uniformity. Notably, the OCE configuration shows a faster reduction in surface-to-center non-uniformity for the upper block, indicating an advantage in achieving thermal stability in this specific direction of heating. However, for the lower block, the OCE configuration results in a slower reduction of non-uniformity, highlighting the variability in performance based on block position and heating direction.

Fig. 9(c) illustrates the evolving temperature disparities at the centers of the two blocks during the heat treatment process across four different layouts. The center temperature differential is obtained by subtracting the temperature of the center of the upper block from the lower one. Initially, the center of the upper block was approximately 45 °C cooler compared to the lower block. However, as the heat treatment advanced, this temperature gap was not only mitigated but also reversed, particularly noticeable in the OCE layout. In this layout, the temperature at the center of the upper block exceeded that of the lower block by about 56 °C after 8 h. In contrast, the other layouts, namely AWICE, AFWE, and TSWE-70, displayed smaller differences in the center temperatures of the blocks over time.

Comparing this with Fig. 9(b), it is evident that the OCE layout not only exhibits high surface-to-center temperature differentials but also large discrepancies between the centers of the blocks, particularly for the lower block. This reinforces the observation that the OCE layout is less effective in providing uniform heating, both on the surface and internally. The significant temperature differential in the OCE layout can be attributed to the direct exposure of the upper block to heating from the top, which causes uneven heating between the upper and lower blocks.

The AWICE and AFWE layouts, while showing intermediate performance, still exhibit higher temperature discrepancies than TSWE-70 but lower than OCE. The AWICE and AFWE layouts, while showing intermediate performance, still exhibit higher temperature discrepancies than TSWE-70 but lower than OCE. AWICE shows considerable center temperature differentials compared to TSWE-70 and AFWE because it also includes the ceiling equipped with heating elements like OCE, so the upper block receives more heat from the top direction. However, its maximum is lower than OCE because in AWICE, in addition to the ceiling, all four side walls are equipped with heating elements, so at any moment, the ceiling elements have a lower portion of heat to emit.

On the other hand, the TSWE-70 layout shows the smallest and most stable temperature discrepancies between the block centers, indicating a more uniform heat distribution throughout the blocks. This is consistent with the findings from Fig. 9(a) and (b), where TSWE-70 also demonstrated better performance in minimizing temperature non-uniformities and differentials.

Overall, these observations highlight the impact of different furnace designs on the thermal history of each block, despite being part of the same batch and subject to the same heat treatment schedule. The TSWE-70 configuration consistently demonstrates superior performance in maintaining uniform temperatures, both on the surface and internally, leading to more consistent mechanical properties in the treated blocks.

Table 4 compares the maximum values experienced for each of the vital parameters in each of the layouts relative to layout TSWE-70. It can be seen that alternative layouts, compared to the optimal layout, result in an increase in maximum surface non uniformities ranging from 4.2 % to 6.6 %. Furthermore, the surface-to-center temperature difference within the blocks increases from 2.2 % to 6.3 %. Such surface temperature non uniformity along with surface-to-center temperature non-uniformities within each block in a batch result in different zones undergoing varied thermal histories. This variation implies that each zone is exposed to varying temperatures for different durations during the non-isothermal cycle. Such differential thermal exposure can result in inconsistencies in mechanical properties across the blocks [43,44], which can ultimately be attributed to the furnace's design.

However, the significant point of interest in this table pertains to the temperature difference at the center of the blocks. As observed, the use of AFWE, AWICE, and OCE configurations results in progressively higher temperature differences at the center of the blocks. For example, in layout OCE, which is a common pattern for heating elements placement in electric furnaces [17], this temperature difference has increased by up to 49 % compared to the TSWE-70 configuration. This substantial increase highlights the inefficiency of the OCE layout in providing uniform heating, likely due to the predominant top heating leading to significant thermal gradients.

Despite the discussed superior performance in TSWE-70, it's crucial to note that this configuration also exhibits considerable surface temperature non-uniformity and a noteworthy difference from the surface to the center. More importantly, there's a significant temperature discrepancy between the centers of the blocks, even though identical final properties are expected for both of them.

A further confirmation of the above analysis is illustrated in Fig. 10 where a cross-sectional temperature contour of the loaded blocks in the furnace with TSWE-70 configuration at the final moment of the non-isothermal cycle (after 27.8 h from the start of the process) is depicted. It can be seen that the majority of the volume of the upper block, particularly its center as indicated by the dashed lines, is about the target temperature. In contrast, the center point of the lower block and a large surrounding area is approximately 10 °C cooler. This indicates unequal energy absorption by these two blocks, underscoring the need for improvement in furnace design to achieve optimal performance.

To address these discrepancies, the next phase of the study involved fine-tuning the coverage area of the side walls by heating elements within the TSWE configuration. This adjustment aimed to optimize thermal uniformity while retaining the existing setup, which is preferred by industrial partner for its practicality and cost-effectiveness. Specifically, this fine-tuning process involves adding or removing rows of heating elements along the furnace's side walls, making it a practical and cost-effective solution for improving thermal uniformity without necessitating a complete overhaul of the existing furnace design.

Table 4
Percentage deviations of performance parameters for each layout compared to TSWE-70.

Layouts	Maximum surface temperature non-uniformity-UB	Maximum surface temperature non-uniformity-LB	Maximum surface-to-center temperature differential-UB	Maximum surface-to-center temperature differential-LB	Maximum centers temperature differential
AFWE	+4.8	+6.6	+4.4	+5.4	+3.9
AWICE	+5.2	+6.3	+3.9	+5.5	+15.4
OCE	+4.6	+4.2	+2.2	+6.3	+49.1

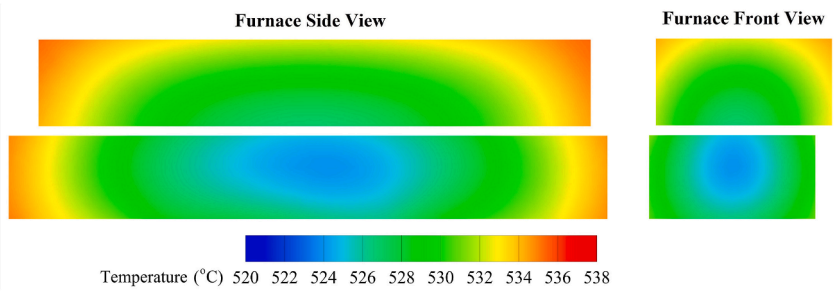

Fig. 10. Temperature contour of loaded blocks at the central cross-section at t = 100,000 s (End of non-iso thermal cycle) for TSWE-70.

5.3. Phase-2 analysis

As outlined in Section 3, the second phase of this study focused on determining the optimum percentage of side wall coverage by the heating elements, examining seven distinct cases. These cases involved varying the coverage percentages on the two side walls to 10 %, 20 %, 30 %, 50 %, 70 %, 90 %, and 100 %. This phase aimed to analyze the dependency of key performance parameters on the extent of wall coverage by the heating elements. Ultimately, this will aid in determining the optimal coverage for achieving uniform thermal conditions.

As illustrated in Fig. 11, the following parameters are presented in a normalized form as a function of wall coverage percentage by heating elements: maximum surface temperature non-uniformity of the upper and lower blocks, maximum surface-to-center temperature differential of the upper and lower blocks, required time for the upper and lower block centers to reach the target temperature, and centers temperature differential. The purpose of normalizing these values is to prevent any single objective from overpowering the others due to scale differences, accelerate convergence in iterative optimization methods, and facilitate clearer interpretation of variable importance [45].

Table 5 indicates the accuracy of the extracted polynomial functions for each of the performance parameters, relative to the extent of wall coverage with heating elements. The data reveals a strong fit for the polynomial models, as evidenced by the high R-squared values and low mean square errors (MSE) across all parameters. The R-squared value, or R-sq%, is particularly important as it represents the percentage of variation in the response that is explained by the model [46,47]. Notably, the minimum R-squared value observed is 97.88 % for the surface temperature non-uniformity of the lower block, which still indicates a highly significant

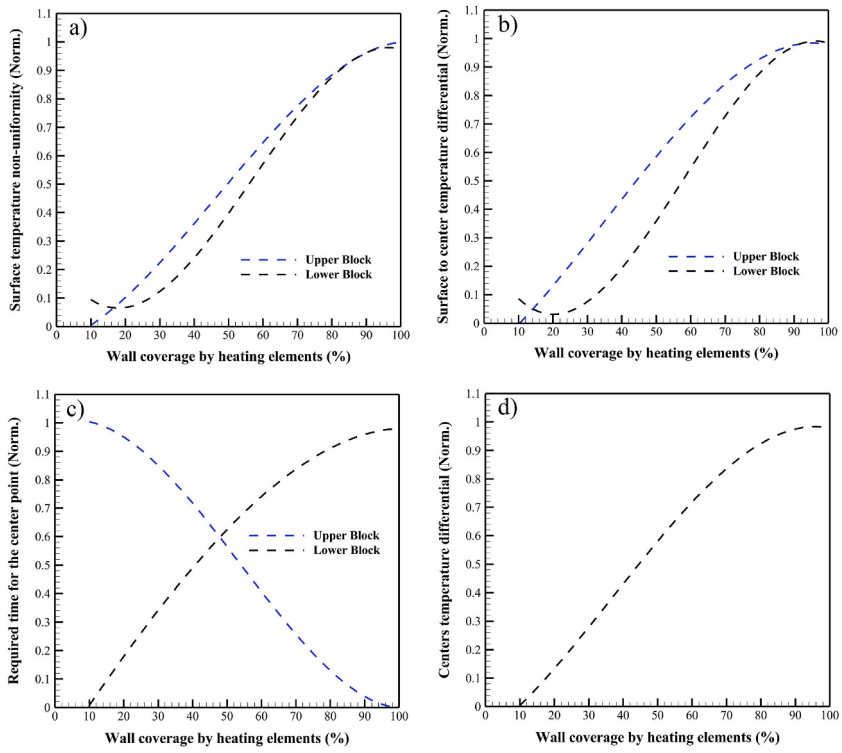

Fig. 11. Polynomial regression curves of blocks thermal parameters vs. wall coverage by heating elements: a) surface temperature non-uniformity of the blocks b) surface-to-center temperature differential c) required time for the blocks' center to touch the target temperature d) centers temperature differential.

Table 5
Accuracy of the extracted polynomial functions for performance parameters.

Formulated objective functions as a dependency on wall coverage by heating elements	R-sq %	MSE
Surface temperature non-uniformity of the upper block	99.60	0.0014
Surface temperature non-uniformity of the lower block	97.88	0.0077
Surface-to-center temperature differential of the upper block	99.85	0.0005
Surface-to-center temperature differential of the lower block	98.63	0.005
Centers temperature differential	99.53	0.0015
Required time for the upper block center to touch the target temperature	99.57	0.0017
Required time for the lower block center to touch the target temperature	99.46	0.0016

model fit. Conversely, the mean square error (MSE) is a measure of the variation that the model does not capture, with the highest MSE being 0.0077 for the same parameter. This suggests that while the model is highly predictive, there are a small degree of variations that it does not account for [48]. In general, the present acceptable degrees of fit suggest that the polynomial functions are highly effective in predicting the thermal behavior of the blocks under various conditions of wall coverage by heating elements.

Fig. 11(a–d) present the thermal behaviors of the upper and lower blocks in relation to the heating element's wall coverage.

In Fig. 11(a), the normalized surface temperature non-uniformity as a function of the wall coverage percentage by heating elements is depicted for both upper and lower blocks. The surface temperature non-uniformity of the upper block (blue curve) starts at 0 at 10 % coverage, indicating an optimal situation for the upper block in terms of surface non-uniformity. This value steadily increases, reaching a normalized value of 1 at 100 % coverage. Conversely, the lower block (black curve) begins at 0.1 at 10 % coverage, decreases to a minimum near 0.06 at about 20 % coverage, and then follows a similar upward trend to the upper block, also reaching 1 at 100 % coverage. Overall, both curves follow a similar trend. The lower non-uniformity at lower coverage levels, especially for the lower block, can be attributed to the more effective distribution of heat at these levels, which balances the surface temperatures. At 20 % coverage, approximately three-quarters of the lower block's side surfaces and all the skids are directly faced to the heating elements, resulting in a more balanced temperature distribution. As coverage increases, the additional heating elements expose more block surfaces directly, leading to increased non-uniformity due to uneven heat distribution. This underscores the importance of optimizing wall coverage by heating elements to achieve uniform surface temperatures.

In Fig. 11(b), the normalized surface-to-center temperature differential as a function of the wall coverage percentage by heating elements is shown for both upper and lower blocks. The upper block's differential (blue curve) starts at 0 at 10 % coverage and steadily increases, reaching a normalized value of 1 at 100 % coverage. On the other hand, the lower block's differential (black curve) begins at 0.1 at 10 % coverage, decreases to a minimum near 0.03 at about 20 % coverage, and then rises similarly to the upper block, also reaching a normalized value of 1 at 100 % coverage. When comparing this to Fig. 11(a), which depicts the normalized surface temperature non-uniformity, it is observed that both parameters exhibit similar trends in response to changes in wall coverage by heating elements. This similarity suggests a consistent underlying thermal behavior influenced by the distribution of heating elements. As wall coverage increases, both surface temperature non-uniformity and surface-to-center temperature differential tend to increase, indicating that more extensive heating element coverage leads to greater thermal gradients within the blocks.

In Fig. 11(c), the normalized required time for the center points of the upper and lower blocks to reach the designated temperature is depicted as a function of the wall coverage percentage by heating elements. The upper block's required time (blue curve) starts at a normalized value of 1 at 10 % coverage, indicating that this coverage requires the most time for the upper block to reach the target temperature. As the coverage increases, the required time decreases, reaching a normalized value of 0 at 100 % coverage, indicating the least time required. Conversely, the lower block's required time (black curve) starts at a normalized value of 0 at 10 % coverage, showing that this coverage requires the least time for the lower block to reach the target temperature, and increases to a normalized value of 1 at 100 % coverage, indicating the most time required. This inverse relationship between the two blocks can be attributed to the distribution of heat within the furnace. At lower coverage levels, the heating elements primarily affect the lower block, which is closer to the heat source, resulting in quicker heating. As the coverage increases, the heat is distributed more evenly across the furnace, and the upper block benefits from increased exposure, leading to a decrease in the required time to reach the designated temperature. Therefore, achieving optimal thermal uniformity required fine-tuning the coverage percentage, which is discussed in detail in the next section (5.4).

In Fig. 11(d), the normalized temperature differential at the centers of the two blocks is depicted as a function of the wall coverage percentage by heating elements. The curve starts at 0 at 10 % coverage, indicating the best situation with the least central temperature difference experienced by the centers of the two blocks over the process. As the wall coverage increases, the temperature differential increases steadily, reaching a normalized value of 1 at about 100 % coverage, indicating the worst situation with the highest maximum central temperature differential. This steady increase in temperature differential can be attributed to the distribution of heat within the furnace. As explained in Fig. 11(a), at lower coverage levels, the heat is more effectively concentrated around the blocks, promoting a more uniform temperature distribution. As the coverage increases, the additional heating elements expose more block surfaces directly, leading to uneven heat distribution and greater temperature differentials at the centers of the blocks. This trend underscores the importance of optimizing the wall coverage by heating elements to achieve uniform internal temperatures within the batch of products.

5.4. Optimization results comparison

Building on the polynomial representations constructed to model the performance parameters as a function of the wall coverage by the heating elements in the Phase-2 Analysis, advanced multi-objective optimization algorithms were subsequently utilized to determine the optimal wall coverage percentages that concurrently minimize these polynomial representations.

Among the seven polynomial curves, four show their minimum at 10 % coverage, two at approximately 20 %, and one at 100 %. This distribution, along with considering equal importance for all objectives, influences the genetic algorithm to select 10 % as the optimal coverage due to its systematic approach to multi-objective optimization. Similarly, the Pareto search algorithm, which balances trade-offs differently, selected 14.2 % as the optimal coverage. Both algorithms converged on optimal values ranging narrowly from 10 % to 14.2 %, which markedly deviates from the original 70 % wall coverage, suggesting a critical reassessment of the conventional layout.

Table 6 presents a comparative analysis, indicating performance improvements at both optimized wall coverage percentages when benchmarked against the baseline condition (TSWE-70). The enhancements achieved by both algorithms are notably close, despite the differences in their methodological approaches and the multifaceted trade-offs involved, as depicted in Fig. 11.

Based on Table 6 values, the improvements at the selected optimum wall coverages are almost the same. However, the 10 % wall coverage determined by the genetic algorithm was slightly more effective in reducing temperature differentials for the upper block, whereas the 14.2 % wall coverage identified by the Pareto search algorithm provided slightly better results in minimizing temperature differentials for the lower block.

Comparative analysis shows that the 10 % coverage is about 4.5 % better in temperature uniformity across the batch of products compared to the 14.2 % coverage. This finding is particularly significant from a products manufacturing point of view, as it promises more consistent products quality.

These optimizations suggest that adjusting the wall coverage percentage by heating elements in the TSWE layout can result in a substantial reduction in performance anomalies. Specifically, surface non-uniformities and surface-to-center temperature differentials can be expected to decrease by 4.0–7.8 percent, and centers temperature differential can reduce by as much as 70.6 percent. Such rectifications promise notable enhancements in the homogeneity of final properties across individual blocks and an entire batch of products.

Fig. 12 depicts the temperature contours within two large blocks at the 50,000-s moment, or approximately one-third of the total tempering process duration, offering insights into the temperature distribution across the mid-cross-section influenced by varied walls coverage by heating elements.

Fig. 12(a) illustrates the result of heating elements layout with 10 % wall coverage, revealing a gradual and even temperature gradient from the surface to the center of both blocks. This is characterized by a predominant temperature span of 435 °C–485 °C in both blocks, with notably similar central temperatures indicating a uniform heat distribution beneficial for the tempering process. In contrast, the 70 % wall coverage layout result shown in Fig. 12(b), which represents the original condition, exhibits a wider tempera-

Table 6
Percentage deviations of performance parameters for each case compared to TSWE-70.

Wall Coverage	Maximum surface non-uniformity-UB	Maximum surface non-uniformity-LB	Maximum surface-to-center temperature differential-UB	Maximum surface-to-center temperature differential-LB	Maximum centers temperature differential
10 %	−7.8	−4.0	−5.8	−5.9	−70.6
14.2 %	−7.4	−4.2	−5.5	−6.2	−66.1

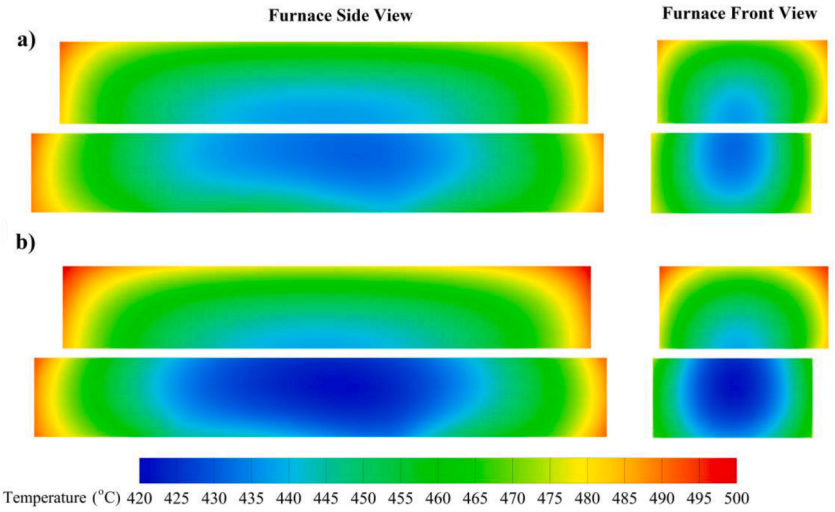

Fig. 12. Temperature contour of loaded blocks at the central cross-section at t = 50,000 s (one-third of total process duration): a) TSWE-10 b) TSWE-70.

ture spectrum across the surfaces, particularly for the lower block, ranging from approximately 420 °C to nearly 500 °C. Moreover, the temperatures at the center of the two blocks differ markedly, reflecting a pronounced thermal imbalance. These variations underscore the enhanced heating performance achieved through the TSWE-10 layout, which promotes a more homogeneous temperature field during the non-isothermal tempering cycle, as opposed to the disparate conditions observed with the original heating elements configuration. These insights could inform not only the design of new furnaces but also the development of future tempering process cycles, leading to reduced non-uniformities in heat treated materials by ensuring a more homogenous thermal profile.

6. Conclusions

In the present investigation, the influence of heating elements layout on the uniformity and quality of heat-treated products in an industrial-scale electrical tempering furnace was examined using a combination of experimental and simulation tools. The key insights are.

1. The developed CFD model, incorporating the turbulence k-ε realizable model, DO radiation model, MRF model, and pre-calculated, temperature-dependent thermophysical properties, has proven to be a reliable representation of the electric heat treatment furnace under investigation.
2. The current layout of the heating elements, two Side walls equipped (TSWE) with heating elements, exhibits the lowest surface non-uniformities and minimized surface-to-center temperature differential for both blocks compared to other typical layouts for this furnace type.
3. The TSWE layout demonstrates the smallest differential in centers temperature for a batch of products at any given moment, compared to other investigated layouts.
4. Correlation between the performance parameters of the electric furnace and the walls' coverage by heating elements was determined.
5. Through the use of multi-objective optimization algorithms, optimal coverage values for the furnace's side walls by the heating elements were identified, ranging from 10 % to 14.2 %. This finding significantly diverges from the conventional 70 % wall coverage, necessitating a critical reassessment of the standard layout.

In future research, the metallurgical aspects of the improved tempering process in an electric furnace will be explored to achieve a better understanding of heat treatment processes.

Data availability

The data that has been used is confidential.

Funding

This research was financially supported by Mitacs under the grant [IT27097].

CRediT authorship contribution statement

Sajad Mirzaei: Writing – review & editing, Writing – original draft, Visualization, Validation, Methodology, Formal analysis, Data curation, Conceptualization. **Nima Bohlooli Arkhazloo:** Writing – review & editing, Methodology. **Jean-Benoit Morin:** Writing – review & editing, Resources. **Mohammad Jahazi:** Writing – review & editing, Supervision, Resources, Project administration, Funding acquisition, Conceptualization.

Declaration of competing interest

The authors declare the following financial interests/personal relationships which may be considered as potential competing interests: Sajad Mirzaei reports financial support was provided by Mitacs Canada. If there are other authors, they declare that they have no known competing financial interests or personal relationships that could have appeared to influence the work reported in this paper.

Acknowledgments

The authors express their sincere appreciation to Finkl Steel, particularly the research and development and heat treatment teams, for supplying the large blocks and for their contributions in instrumentation and measurements for this research. Special thanks to the Digital Research Alliance of Canada for providing access to high-performance clusters, vital for our high-computational simulations, and their great support team.

Data availability

The data that has been used is confidential.

References

[1] G.E. Totten, Steel Heat Treatment: Metallurgy and Technologies, CRC press, 2006.
[2] L.C.F. Canale, et al., A historical overview of steel tempering parameters, Int. J. Microstruct. Mater. Prop. 3 (4/5) (2008).
[3] I.D. Palacio-Caro, P.N. Alvarado-Torres, L.F. Cardona-Sepúlveda, Numerical simulation of the flow and heat transfer in an electric steel tempering furnace, Energies 13 (14) (2020).
[4] J. Smolka, A.J. Nowak, D. Rybarz, Improved 3-D temperature uniformity in a laboratory drying oven based on experimentally validated CFD computations, J. Food Eng. 97 (3) (2010) 373–383.
[5] M. Filipponi, et al., Thermal analysis of an industrial furnace, Energies 9 (10) (2016) 833.
[6] Z. Fu, et al., A new modelling method for superalloy heating in resistance furnace using FLUENT, Int. J. Heat Mass Tran. 128 (2019) 679–687.
[7] P.M. Angelopoulos, A. Peppas, M. Taxiarchou, Modelling the thermal treatment and expansion of mineral microspheres (perlite) in electric furnace through computational fluid dynamics (CFD): effect of process conditions and feed characteristics, Miner. Process. Extr. Metall. Rev. (2023) 1–18.
[8] S. Mirzaei, et al., Influence of spacers and skid sizes on heat treatment of large forgings within an industrial electric furnace, Energies 16 (7) (2023) 2936.
[9] S.A. Tan, K.H. Yu, M.Z. Abdullah, Heat transfer analysis on wafer annealing process in semiconductor multi-wafer furnace using CFD simulation, J. Mech. Sci. Technol. 36 (6) (2022) 3143–3151.
[10] C.O. Díaz-Ovalle, et al., An approach to reduce the pre-heating time in a convection oven via CFD simulation, Food Bioprod. Process. 102 (2017) 98–106.
[11] Finkl Steel Inc. Saint-Joseph-de-Sorel, QC, Canada.; Available from:: http://www.sorelforge.com/.
[12] N.B. Arkhazloo, et al., Experimental and unsteady CFD analyses of the heating process of large size forgings in a gas-fired furnace, Case Stud. Therm. Eng. 14 (2019) 100428.
[13] UNIFRAX, Product information sheet, in: Fiberfrax®Blanket and Mat Products, 2017 USA.
[14] I. Standard, Temperature Measurement Thermocouples, 1982.
[15] N.B. Arkhazloo, et al., Determination of temperature distribution during heat treatment of forgings: simulation and experiment, Heat Tran. Eng. (2021) 1–24.
[16] N. Bohlooli Arkhazloo, et al., Optimization of furnace residence time and loading pattern during heat treatment of large size forgings, Int. J. Adv. Des. Manuf. Technol. 113 (9–10) (2021) 2447–2460.
[17] A. Kanthal, Kanthal Super–electric Heating Element Handbook, 1999 Sweden.
[18] G. Coskun, et al., Optimization of the injectors position for an electric arc furnace by using CFD simulation, J. Appl. Fluid Mech. 16 (2) (2022) 233–243.
[19] ANSYS Inc, ANSYS fluent mosaic technology automatically combines disparate meshes with polyhedral elements for fast, accurate flow resolution, Available from: https://www.ansys.com/content/dam/resource-center/white-paper/ansys-fluent-mosaic-technology-wp.pdf, 2020 8 July 2024.
[20] V.M. Arocena, L.A.M. Danao, Improving the modeling of pressure pulsation and cavitation prediction in a double-volute double-suction pump using mosaic meshing technology, Processes 11 (3) (2023) 660.
[21] B. Hadała, Z. Malinowski, M. Rywotycki, Energy losses from the furnace chamber walls during heating and heat treatment of heavy forgings, Energy 139 (2017) 298–314.
[22] ANSYS, ANSYS Fluent Theory Guide, 2022 R2, ANSYS, Inc.: Southpointe, 2600 Ansys Drive, Canonsburg, PA 15317, USA.
[23] J.P. Van Doormaal, G.D. Raithby, Enhancements of the SIMPLE method for predicting incompressible fluid flows, Numer. Heat Tran. 7 (2) (1984) 147–163.
[24] T.-H. Shih, et al., A new k-ϵ eddy viscosity model for high Reynolds number turbulent flows, Comput. Fluid 24 (3) (1995) 227–238.
[25] M.B. Dogruoz, G. Shankaran, Computations with the multiple reference frame technique: flow and temperature fields downstream of an axial fan, Numer. Heat Tran., Part A: Applications 71 (5) (2017) 488–510.
[26] H.K. Versteeg, W. Malalasekera, An Introduction to Computational Fluid Dynamics: the Finite Volume Method, Pearson education, 2007.
[27] A. Jamaluddin, P. Smith, Predicting radiative transfer in rectangular enclosures using the discrete ordinates method, Combust. Sci. Technol. 59 (4–6) (1988) 321–340.
[28] M. Nakhaei, et al., CFD modeling of gas–solid cyclone separators at ambient and elevated temperatures, Processes 8 (2) (2020) 228.
[29] SenteSoftware, JMatPro Users Guide 6.2.1. Sente Software Ltd.:The Technology Centre Surrey Research Park, Guildford, United Kingdom.
[30] B. Mayr, et al., CFD analysis of a pusher type reheating furnace and the billet heating characteristic, Appl. Therm. Eng. 115 (2017) 986–994.
[31] G. Tang, et al., Modeling of the slab heating process in a walking beam reheating furnace for process optimization, Int. J. Heat Mass Tran. 113 (2017) 1142–1151.
[32] L. Qiu, et al., Three-dimensional fluid-solid coupling heat transfer simulation based on the multireference frame for a side-blown aluminum annealing furnace, Engineering Applications of Computational Fluid Mechanics 13 (1) (2019) 1036–1048.
[33] M.L. Lavadera, et al., A combined experimental, numerical, and data consistency approach for the characterization of temperature distribution in a MILD combustion furnace, Appl. Therm. Eng. (2024) 122625.
[34] G. Wang, Y. Li, Effects of alloying elements and temperature on thermal conductivity of ferrite, J. Appl. Phys. 126 (12) (2019).
[35] M. Matlab, Version R2021b. MathWorks, 2021.
[36] S. Sivanandam, et al., Genetic Algorithms, Springer, 2008.
[37] A.J. Umbarkar, P.D. Sheth, Crossover operators in genetic algorithms: a review, ICTACT journal on soft computing 6 (1) (2015).
[38] K. Deb, Multi-objective optimisation using evolutionary algorithms: an introduction, in: Multi-objective Evolutionary Optimisation for Product Design and Manufacturing, Springer, 2011, pp. 3–34.
[39] M. Fleischer, The measure of Pareto optima applications to multi-objective metaheuristics, in: International Conference on Evolutionary Multi-Criterion Optimization, Springer, 2003.
[40] N.B. Arkhazloo, Optimization of furnace residence time and ingots positioning during the heat treatment process of large size forged ingots. École de Technologie Supérieure, Université du Québec, 2020.
[41] W. Ji, et al., Modeling and determination of total heat exchange factor of regenerative reheating furnace based on instrumented slab trials, Case Stud. Therm. Eng. 24 (2021) 100838.
[42] D. Wang, et al., Analysis of billet temperature non-uniformity in a regenerative reheating furnace: considering periodic combustion switching and misalignment contact of walking beams, Case Stud. Therm. Eng. (2024) 104573.
[43] M. Gao, C.N. R, M. Jahedi, Y. Li, Estimating equilibration times and heating/cooling rates in heat treatment of workpieces with arbitrary geometry, J. Mater. Eng. Perform. 9 (1) (2000) 62.
[44] J. Kang, Y. Rong, Modeling and simulation of load heating in heat treatment furnaces, J. Mater. Process. Technol. 174 (1–3) (2006) 109–114.
[45] L. He, et al., A survey of normalization methods in multiobjective evolutionary algorithms, IEEE Trans. Evol. Comput. 25 (6) (2021) 1028–1048.
[46] A. Rabiee, et al., Multi-objective optimization of rectangular microchannel heat sink based on entropy generation and hydro-thermal performance using NSGA-II algorithm, Int. Commun. Heat Mass Tran. 149 (2023) 107140.
[47] D. Chicco, M.J. Warrens, G. Jurman, The coefficient of determination R-squared is more informative than SMAPE, MAE, MAPE, MSE and RMSE in regression analysis evaluation, PeerJ Computer Science 7 (2021) e623.
[48] E. Ostertagová, Modelling using polynomial regression, Procedia Eng. 48 (2012) 500–506.